The Impact of Smoke on the Ultraviolet and Visible Radiative Forcing Under Different Fire Regimes

Authors: Park, Yun H, Sokolik, Irina N, and Hall, Samuel R

Source: Air, Soil and Water Research, 11(1)

Published By: SAGE Publishing

URL: https://doi.org/10.1177/1178622118774803

The Impact of Smoke on the Ultraviolet and Visible Radiative Forcing Under Different Fire Regimes

Air, Soil and Water Research
Volume 11: 1–10
© The Author(s) 2018
DOI: 10.1177/1178622118774803
SAGE

Yun H Park[1], Irina N Sokolik[1] and Samuel R Hall[2]

[1]School of the Earth and Atmospheric Sciences, Georgia Institute of Technology, Atlanta, GA, USA. [2]National Center for Atmospheric Research, Boulder, CO, USA.

ABSTRACT: The quantification of the UV characteristics of smoke aerosols is valuable to UV Index forecasting, air quality studies, air chemistry studies, and assessments of the impacts on regional and global environmental changes. The wavelength dependence of the light absorption by smoke aerosol has been researched throughout the UV and visible spectral region and varies with fire type and aerosol composition. An objective of this study is to investigate the spectral optical properties (eg, extinction coefficient, single-scattering albedo, and asymmetry parameter), UV actinic fluxes, and radiative forcing of smoke of different fire regimes. The smoke aerosol information (eg, simulated smoke fields from biomass burning emission and vertical distribution of the mass concentration of smoke components) from WRF-Chem is used to distinguish 2 smoke types: flaming and smoldering. To compute the spectral optical properties for the fire regimes, the representative size distribution and spectral refractive index have been implemented into the Mie code, and the optical properties are used to run the tropospheric ultraviolet and visible radiative transfer model. We make comparisons between simulated model and measured actinic flux in the UV and visible spectra under smoke aerosol laden conditions. The WRF-Chem-SMOKE model simulates the smoke plume matched with fire locations and comparable aerosol optical depth (AOD) with satellite measurements. However, the correlation between the simulated and observed AOD is small, which implies that adjusting the fire size for the emission inputs and improving meteorological fields are required for further research. The smoke at selected locations reduces the UV actinic flux and increases the visible actinic flux above the plume at small solar zenith angles. The specific spectral response is dependent on the smoke type. Overall, the results of this investigation show that this approach is valuable to estimate the impact of smoke on UV and visible radiative fluxes.

KEYWORDS: Smoke aerosols, impacts on UV radiation, modeling, aircraft and satellite data analysis

RECEIVED: October 23, 2017. **ACCEPTED:** March 28, 2018.

TYPE: Original Research

FUNDING: The author(s) disclosed receipt of the following financial support for the research, authorship, and/or publication of this article: This research was supported, in part by the NASA Radiation Program and NASA Atmospheric Chemistry Program, grant number NNX16AH69G, and NSF, grant number 1637279. The data used in this study are available upon request.

DECLARATION OF CONFLICTING INTERESTS: The author(s) declared no potential conflicts of interest with respect to the research, authorship, and/or publication of this article.

CORRESPONDING AUTHOR: Irina Sokolik, School of Earth & Atmospheric Sciences, Georgia Institute of Technology, 311 Ferst Drive Atlanta, GA 30332-0340, USA. Email: irina.sokolik@eas.gatech.edu

Introduction

Biomass burning is one of the largest contributors of both gaseous and particulate emissions to the atmosphere resulting in 34% to 38% of total carbonaceous aerosol emissions.[1] Smoke aerosols affect the solar and UV radiation through various interactions. The direct effect of most smoke types is to increase atmospheric reflectivity. However, due to the complex interactions between the aerosols and the physical and chemical components of the Earth's climate system, our understanding of their role in climate change remains uncertain.[2,3]

The direct aerosol radiative effect has been estimated from satellite and surface-based measurements.[4] However, the Intergovernmental Panel on Climate Change[1] reports that despite the significant progress of our understanding of the direct radiative effect, the overall atmospheric impacts of the aerosols, especially from biomass burning, continue to be one of the largest uncertainties in the Earth's energy budget. Climate model studies have found that the positive impact of absorbing aerosols, such as black carbon (BC), originating from wildfires, can be 2 or more times larger than the impact of carbon.[5]

Another consequence of the aerosol direct effect on solar radiation is a decrease in vegetative carbon gain due to a reduction in the total surface photosynthetically active radiation (PAR; 400-700 nm) and a corresponding increase in the diffuse fraction of the PAR.[6-9] Numerous studies have reported the aerosol effect on photolysis rates in the atmosphere. Kobayashi et al[10] showed that the photolysis rates are reduced near the surface due to absorption by carbonaceous aerosols. However, aerosols can also enhance photolysis rates when the scattering of the ultraviolet radiation dominates absorption in aged aerosols.[11]

The light absorption of aerosols from biomass burning varies strongly with wavelength.[12,13] Black carbon and organic carbon (OC) are representative carbonaceous particles of smoke emissions from biomass burnings. The spectrally dependent aerosol imaginary refractive index is driven by the relatively constant imaginary refractive index of BC and the spectrally dependent imaginary refractive index of OC. The compositions and mass fractions of the smoke components vary, depending on the type of the burning fuel, as well as the fire regime (eg, flaming and smoldering), which affects smoke optical properties.[14] In addition, atmospheric conditions control the updraft motion of the smoke emission.

The goal of this study is to investigate smoke impacts on the UV and visible radiative forcing under different smoke-laden conditions. First, we characterize the spectral optical properties of smoke aerosols based on the composition and size distributions. Second, we estimate a change of spectral actinic fluxes for representative smoke types by considering optical properties of

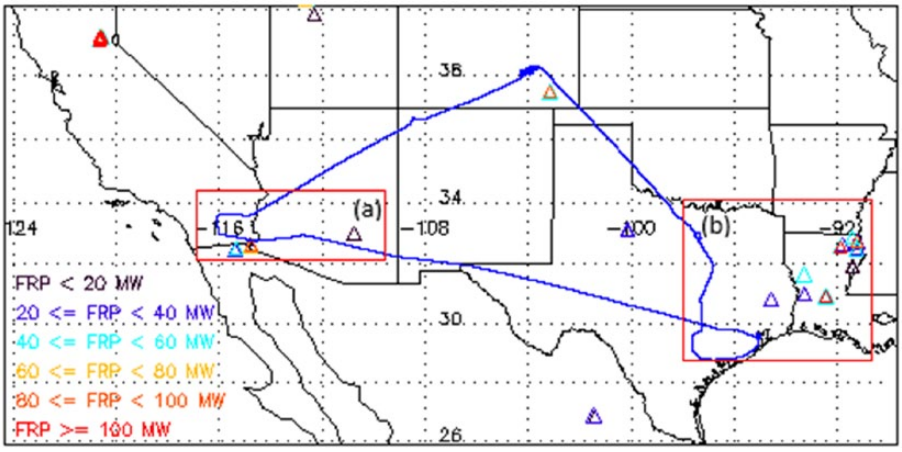

Figure 1. The domain of the study area with the location of aircraft tracking (blue line) and active fire location from MODIS Thermal Anomalies/Fire products (triangle) on August 16, 2013. Two subdomains ((a) and (b)) are selected for the evaluation.

the different smoke types. We select 2 different smoke regimes in this study: flaming and smoldering. The flaming phase uses limited oxygen, resulting in a higher fraction of soot particles. The smoldering phase refers to the flameless, low-temperature combustion, producing more OC[15] that often occurs after the flaming phase decreases. To isolate aerosol effects, this study is confined to cloud-free conditions.

The observational data are described in section "Satellite Remote Sensing and Aircraft Data"; the methodology to estimate UV fluxes in smoke-laden conditions is presented in section "Methodology"; results of the modeling studies and comparisons of fluxes with observations are presented in section "WRF-Chem-SMOKE Modeling"; and the discussion and the summary are given in section "Results and Discussion."

Satellite Remote Sensing and Aircraft Data

MODIS fire products

The MODIS fire observations serve to advance global monitoring of fire process and its effects on ecosystems, the atmosphere, and climate. The MODIS instrument acquires data 4 times a day from the Terra (10:30 AM and 10:30 PM) and Aqua (1:30 PM and 1:30 AM) satellites. We use MOD 14, the level 2 swath data provided daily at 1-km resolution and includes the MODIS Thermal Anomalies/Fire products, primarily derived from the MODIS channels 21 (4 μm) and 31 (11 μm). The fire detection strategy is based on the absolute detection of a fire (when the fire strength is sufficient to detect) and the detection relative to its background (to account for the variability of the surface temperature and the reflection by the sunlight). The science data sets in this product include the fire-mask, algorithm quality, radiative power, and numerous layers, describing fire pixel attributes.

The MODIS fire radiative power (FRP) is widely used to estimate fire emissions. Val Martin et al[16] showed the correlation between plume heights and the MODIS FRP. They reported large FRP (~1600 MW) in the free troposphere and low FRP (<500 MW) within the boundary layer. Freeborn et al[17] showed the MODIS FRP uncertainty in satellite-based active fire characterization and biomass burning estimation, which can limit the confidence in flux estimates at the pixel-by-pixel resolution.

An average of FRP within the domain (Figure 1) is 80 MW with a range of 10 to 2300 MW. Many points more than 500 MW have low confidence (<70%). Kauffman et al (1998)[18] suggested to identify the fire category by the intensity as follows:

C1: FRP < 100 MW;

C2: 100 < FRP < 500 MW;

C3: 500 < FRP < 1000 MW;

C4: 1000 < FRP < 1500 MW;

C5: FRP > 1500 MW.

The fire category distribution in the study domain described below contains more than 85% that are in C1 and C2. We select FRP with the high confidence (>70) and less than 500 MW. When converting to fire size, the 0.5 km^2 corresponds to 500 MW. Figure 1 shows the distribution of FRP with the location of the aircraft flight.

Aircraft data

We have used the data acquired by the Atmospheric Radiation Investigations and Measurements group at the National Center for Atmospheric Research (NCAR) during the field project "Studies of Emissions and Atmospheric Composition, Clouds and Climate Coupling by Regional Surveys" (SEAC4RS). The objectives of this mission included studying modeling results and measurements, to investigate how emissions change in deep convective flows under changing dynamical and chemical conditions, and examining the influences of aerosol particles on

Table 1. The spectral complex refractive index for each smoke component.

λ, NM	REFRACTIVE INDEX					
	OC		BC		SO4	
	REAL	IMAGINARY	REAL	IMAGINARY	REAL	IMAGINARY
350	1.5	0.168	1.45	0.75	1.45	0
400	1.5	0.112	1.5	0.65	1.45	0
450	1.5	0.063	1.54	0.55	1.45	0
500	1.5	0.045	1.59	0.5	1.42	0
550	1.5	0.03	1.63	0.48	1.37	0
600	1.5	0.017	1.62	0.48	1.51	0
650	1.5	0.005	1.62	0.47	1.42	0
700	1.5	0.001	1.61	0.47	1.3	0
References	Kirchstetter et al.[12]		Chang and Charalampopoulos[20]		Massie and Hervig[21]	
Type of burning	SAFARI biomass smoke		Flame soot			

weather and climate. Two aircraft were involved in the project: the NASA DC-8, providing observations from near the surface to 12 km, and the NASA ER-2, providing high-altitude observations extending into the lower stratosphere. The mission was conducted from August to September 2013. The location of the aircraft track for the case study described here is shown in Figure 1 with the blue line along with the location and FRP of fires in the area.

The spectrally resolved actinic flux was measured by the charge-coupled device actinic flux spectroradiometer (CAFS) systems. The CAFS instruments are primarily used to calculate photolysis frequencies in airborne, chemistry-focused missions, including SEAC4RS. However, the spectrally resolved actinic flux can also be exploited for radiative aerosol properties, as in this study.

Methodology

Spectral complex refractive indices of smoke aerosols

The light absorption of OC is strongly wavelength dependent across the UV, whereas BC has relatively linear absorption. Several experiments for examining the spectral optical properties of smoke have been performed. Depending on the sampling method, the real and imaginary parts of refractive indices are different not only in magnitude but also in spectral behaviors. Lee and Tien[19] reported that the real part of the refractive index is decreasing to the wavelength of 0.8 µm and increasing to 3 µm, whereas Chang and Charalampopoulos[20] showed the continuously increasing real part of the refractive index with the increasing wavelength. Kirchstetter et al[12] showed that OC extracted from biomass smoke samples has the imaginary part of the refractive index decreasing with the wavelength. We define the spectral refractive index for OC, BC, and SO4 (350-700 nm) using the data from the following studies: Chang and Charalampopoulos,[20] Kirchstetter et al,[12] and Massie and Hervig[21] (Table 1). Sulfate aerosols attenuate solar radiation by scattering, which is why no value in the imaginary part of the refractive index of sulfate is given, whereas carbonaceous aerosols absorb and scatter the UV and solar radiation.

The optical properties vary depending on smoke types and their components. Reid et al[22] showed the existence of the different fractions of the mass of each component in different types of fires; the BC/OC ratio varies 0.06 to 0.23 for grass/savanna, 0.03 to 0.15 for boreal forest, and 0.08 to 0.2 for tropical forest biomass burning. Also, the fraction between the flaming phase and the smoldering phase forest fires is 40%/60%, savanna/grass is 93%/7%, woody savanna, and cerrado is 75%/25%. We assume that smoke aerosols from the biomass burning consist of BC, OC, and sulfate, and all smoke particles undergo rapid aging within a couple of hours.

WRF-Chem-SMOKE Modeling

The configuration of WRF-Chem-SMOKE

The WRF-Chem-SMOKE model is based on WRF (version 8.1.1), which is widely used for weather forecasting and regional meteorological studies, as well as to simulate gas-phase chemistry, and aerosol-cloud-radiation interactions.[23,24] Studies have shown that WRF-Chem is applicable to a wide range of atmospheric conditions, supported by the in situ and remote sensing data.[25,26] Wang et al[26] showed that when FLAMBE smoke emissions are injected within 800 m above the surface, and good agreement can be found between the WRF-Chem and satellite/ground-based observations of the surface particulate matter mass, the aerosol vertical profile, and the smoke transport path.

Table 2. WRF-Chem model configuration with chemical schemes.

VERSION 3.8.1	CONFIGURATION
Horizontal resolution	9 km
Domain coverage	Southwestern US
Map projection	Mercator
Horizontal grid	349 × 169
Initialization	NARR analysis data
Radiation	RRTM (LW)/Duhia (SE)
Land surface	Noah
Cumulus	Grell-Freitas ensemble
PBL	YSU
Microphysics	Morrison
Chemical driver	RADM2
Aerosol driver	MADE/SORGAM
Biomass burning emissions	MODIS FRP, 3BEM, and plume rise model
Gas chemistry	On
Aerosol chemistry	On
Cloud chemistry	On
Aerosol-cloud-radiation interactions	On

Table 2 lists the model configuration options considered in this study. The domain of our study is the southwestern United States (125W-90W, 27N-40N) with 350 × 170 grid points and the 9 km grid spacing (red rectangles in Figure 1). The 3-hourly, 32 × 32 km North American Regional Reanalysis (NARR) data are used for the initializing and specifying the boundary conditions. The microphysics and cumulus parameterizations used are the Morrison and the Grell-Freitas ensemble scheme, respectively. The Yonsei University (YSU) boundary layer scheme and unified Noah land surface model are used.

The simulation of aerosol processes is performed using the Second-Generation Regional Acid Deposition Model (RADM2) and the Modal Aerosol Dynamics Model for Europe with Secondary Organic Aerosol Model (MADE/SORGAM).[27,28] Because the main reason for using the WRF-Chem for this study is to track smoke from fire emissions, only the background aerosol database is used. No biogenic and anthropogenic emission databases are considered here.

Tropospheric ultraviolet and visible modeling

To estimate the impact of smoke on UV fluxes, we use the 1-dimensional (1D) tropospheric ultraviolet and visible (TUV) radiative transfer model developed at NCAR,[29] which is incorporated in the WRF-Chem-SMOKE model. The TUV version 4.2 includes 115 photo-dissociation reactions with the most recent data on the absorption cross sections and quantum yields, based on regular publications of the evaluation panels for the kinetic data from the NASA Jet Propulsion Laboratory and the International Union of Pure and Applied Chemistry (IUPAC). The radiative transfer model was run in a 2-stream approximation and calculations were performed from 350 to 700 nm. We selected the surface albedo of 0.1 for the UV and visible spectral region because the variation of the surface albedo is insignificant in the spectral region for considered surface types.[30,31]

The selection of smoke aerosol loading conditions

Fire properties, determined by the emission intensity and the thermodynamic stability of the atmosphere, are used to distinguish between a flaming phase and a smoldering phase. The public version of the WRF-Chem model includes a 1D plume rise model developed by Freitas et al,[32] which accounts for these properties. The smoke injection height is calculated by solving governing equations.[32] The ability of the WRF-Chem 1D plume rise model to produce realistic injection heights has been demonstrated by Sessions et al.[33]

We distinguish between flaming and smoldering phases of biomass burning events based on the injection height of the layer of smoke using a simple scheme: if a plume is located below planetary boundary layer (PBL), it represents the smoldering phase; if a plume is located above PBL, it represents the flaming smoke (illustrated on the bottom of Figure 2).

An approach to computing spectral UV/VIS fluxes

To estimate spectral actinic fluxes, the WRF-Chem, Mie code (Lorenz-Mie scattering calculation), and the TUV model are used. The smoke aerosol size distribution and complex refractive index were used to develop aerosol optical models within the UV and visible spectral range. We assume that the smoke consists of OC, BC, and SO_4 with the spectral refractive indices shown in Table 1. The index for each component is provided to the Mie code together with size distribution to calculate the spectral optical properties, including single-scattering albedo (SSA) (ω_0), asymmetry factor (g), and extinction coefficient (k_e). Then, the optics of external mixtures is computed by summing up the weighed (based on the proportion assigned from the WRF-Chem-SMOKE simulation) optical properties of individual species. The optical properties are used as an input in the TUV code to simulate actinic fluxes and irradiances. Figure 2 illustrates the procedure to perform the calculations of radiative impacts of smoke.

Results and Discussion

Validation of simulated smoke plumes with satellite observation data

The simulated smoke from the biomass burning modeled with WRF-Chem-SMOKE is validated before the radiative flux

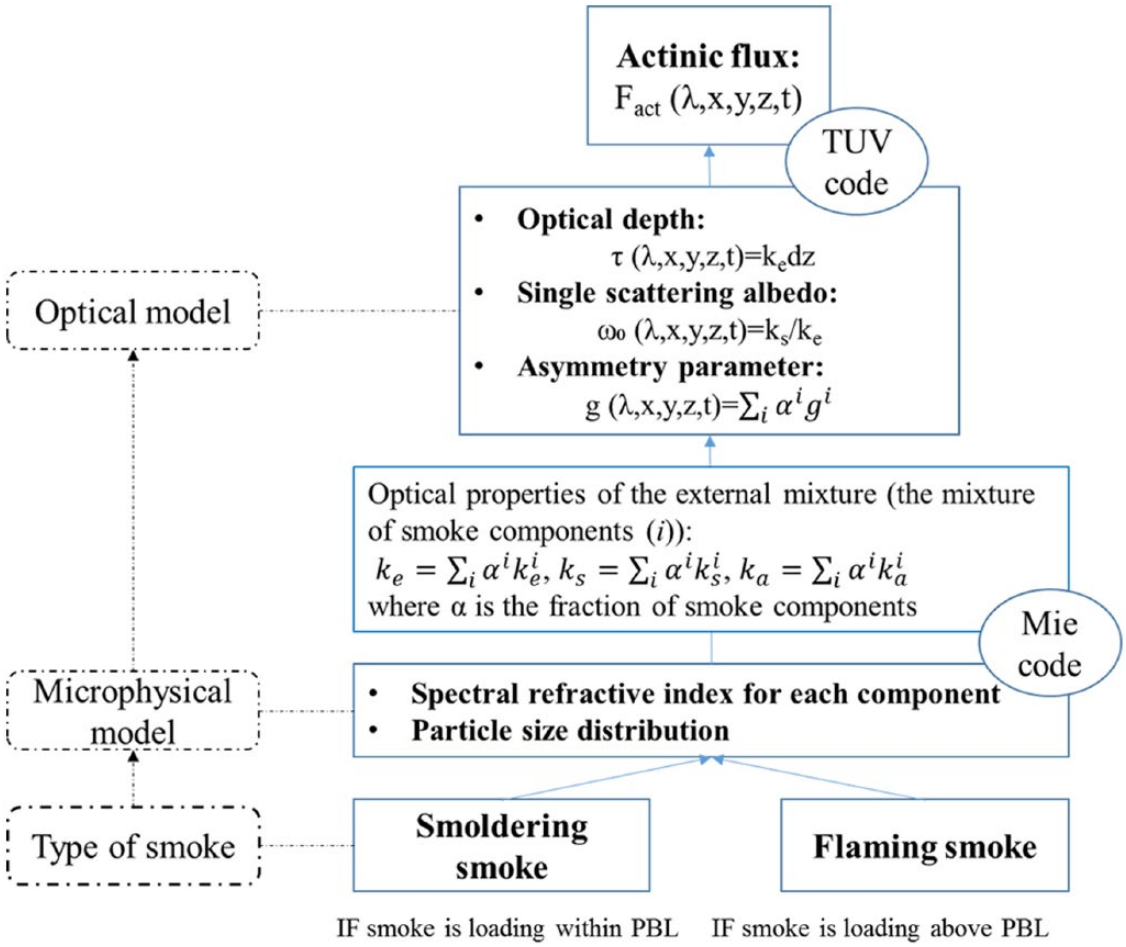

Figure 2. The procedure to perform the calculations of radiative impacts of smoke.

computations are applied. Figure 3 shows MODIS aerosol optical depth (AOD) and simulated AOD for box (a) and (b) in August 16, 2013. There were several fires over southern California and the smoke plumes were transported to Arizona where MODIS measured 0.4 AOD in Arizona (Figure 3A). Figure 3C shows the simulated AOD due to smoke (~0.2) over southern California but the model does not appear to capture the transported plumes. There was high AOD in Louisiana (Figure 3B), matching the fire emission locations (in Figure 1) and the model also simulated high AOD (Figure 3D). Overall, the simulated aerosol spatial distribution matched with the observations, but the correlation by each pixel is low (~0.28) due to the uncertainty of emission data and meteorological fields (eg, wind speed/direction, temperature profiles), as expected. The presence of other aerosol types, ie, the pollution, may also contribute to the low correlation.

Figure 4 shows PM2.5 mass concentrations representing the simulated smoke plumes on August 16, 2013, and it matches to the fire locations used for the emission data shown in Figure 1. Extremely high FRP in northern California and Louisiana is eliminated because most smoke have small FRP (<40 MW). It is noticeable that high smoke plumes are detected in Louisiana, which is corresponding to high AOD in Figure 3. However, it is apparent that smoke concentration from fire emissions is still insufficient to have comparable AOD with the satellite data. The fire size for the emission inputs as well as meteorological fields must be adjusted for the future study.

Analysis of optical properties of smoke types

The analysis of the spectral optical properties of different smoke types assists to understand spectral aerosol characteristics due to light absorption and scattering. Figure 5 shows the averaged extinction coefficient (k_e) and SSA, asymmetry factor (g) for smoldering and flaming phases over land.

The SSA albedo for the flaming smoke is higher than for the smoldering one across the UV and visible wavelengths due to the difference of the fraction of smoke components. As shown in Table 3, flaming smoke has a larger fraction of non-absorbing component, sulfate, and a smaller fraction of absorbing components, OC and BC. This relates to the flaming smoke being loaded above PBL, where it can react and be oxidized by other gases and particles (so called "aged smoke"). The extinction coefficient is larger in the smoldering phase in the visible but larger in the flaming phase in the UV. The difference in the asymmetry factor between the 2 smoke types is insignificant because we assumed the same size distribution for

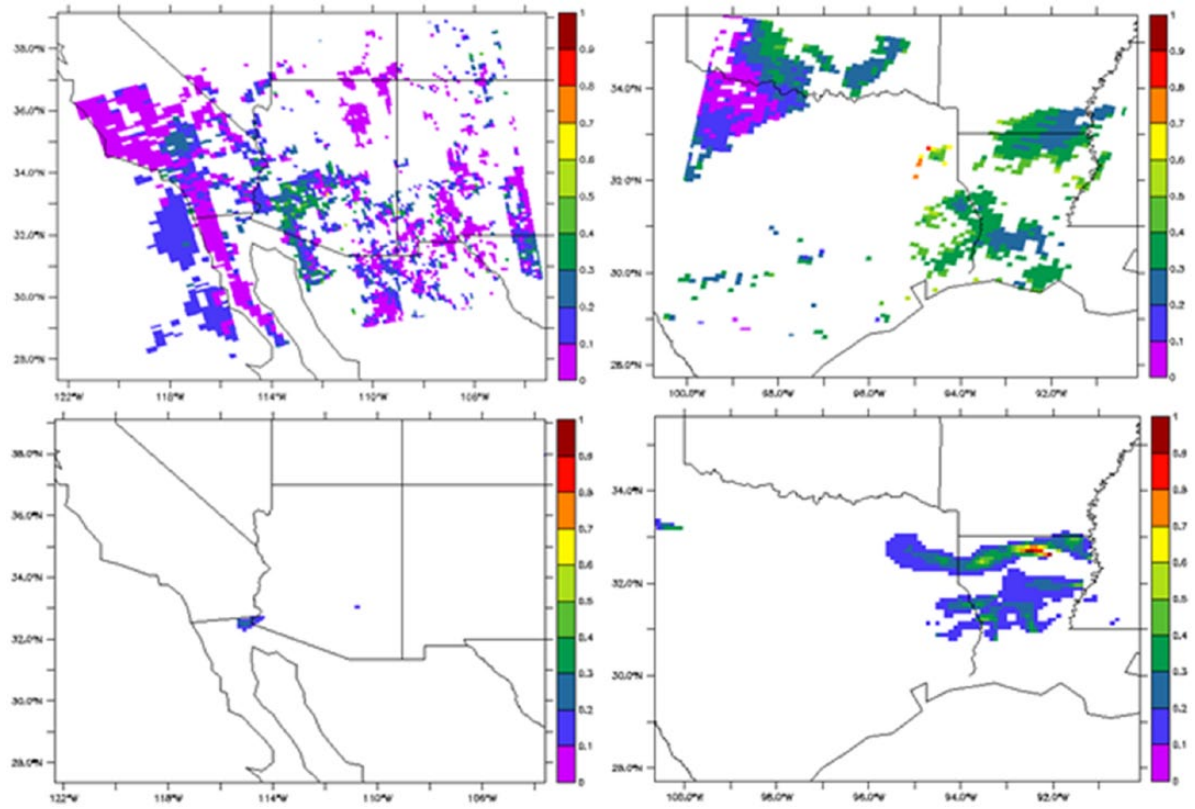

Figure 3. An image of MODIS AOD (top) and simulated AOD (bottom) for box (a) (left) and box (b) (right) on August 16, 2013.

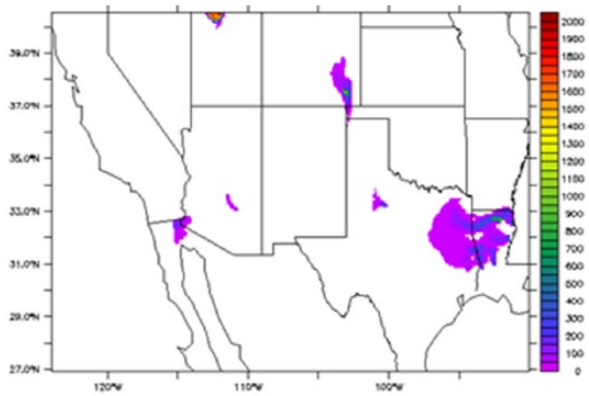

Figure 4. Simulated smoke plume using PM2.5 mass concentration (μm/m^3).

the flaming and smoldering phases. Thus, the scattering angle (forward or backward) is similar.

Comparison of the calculated fluxes with the aircraft data

We select 2 subdomains, box (a) and box (b) in Figure 1, to compare the calculated actinic fluxes with the aircraft data. The aircraft data provide 2 types of actinic fluxes: "nadir" to measure upwelling radiation and "zenith" to measure the downwelling radiation. The net actinic flux defines the sum of direct and diffusive fluxes for all directions. The aircraft passed a location of 32.84N and 115.03W in box (a) at 7.81-km altitude at 17:25 LT and the comparable calculated flux is chosen at the nearest pixel (32.53N, 115.3W) at 7.87-km altitude. As shown in Figure 6A, the calculated net actinic flux (red star) trend increasing with wavelength is well matched with the measurement (black line), which shows the large increment after 400 nm and consistency after 500 nm. The net actinic flux from TUV is underestimated with the largest error in 450 nm (−1014 photons cm^{-2} s^{-1} nm^{-1}), which may be due to less diffusive flux in the atmosphere at the large solar zenith angle (SZA) in the calculation. Simulated AOD is very small (<<0.1), whereas MODIS AOD shows 0.2. The AOD is related to the mass concentration, and the simulated mass concentration is not sufficient to produce the observed actinic flux.

Another location for the validation of the calculated actinic flux is 29.84N and 96.02W at 7.1 km at 14 LT from the aircraft and the nearest pixel (31.04N, 93.23W) of the simulation at 7.77 km in box (b). The calculation has agreement with the observation in net actinic flux. The actinic flux with the increasing wavelength at small solar angle is simulated better than at the large solar angle, which implies the uncertainty of the diffuse flux at 14 LT (SZA: 29°) is less. Simulated AOD and MODIS AOD have both high AOD ~0.4.

The differences in actinic flux between the observation and the calculation (Figure 6) may be due to other aerosol components, which were not included in the calculation. Although the model considers only available aerosols due to biomass

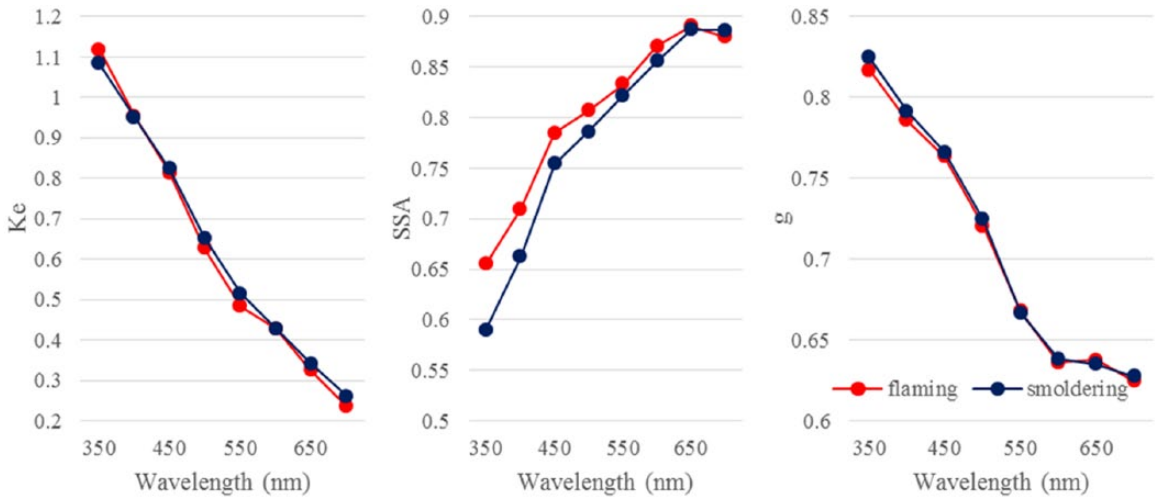

Figure 5. Spectral optical properties for smoldering smoke (blue) and flaming smoke (red) over the land with the standard deviation on August 16, 2013.

Table 3. The averaged fraction of the smoke component for smoke pixels.

	$F_{\_OC}$	$F_{\_BC}$	$F_{\_SO4}$
Flaming	0.74	0.10	0.16
Smoldering	0.87	0.11	0.02

burning, the measured actinic flux will also be affected by aerosols from other natural and anthropogenic sources. The accuracy of the modeled injection height will also affect the comparison. The simulated flaming smoke is loaded at 2 to 4 km at the considered locations, and actual smoke height is about 5 km at 17:25 from the JPL Digital Image Animation Laboratory (DIAL) images (https://science.larc.nasa.gov/lidar/seac4rs/data/20130816_bsr_1064_ff.png). Thus, further analysis related to the injection height and smoke components may be required to reduce the uncertainty of the net actinic flux from the simulation.

Analysis of the change of actinic fluxes caused by smoke

The actinic flux (photons $cm^{-2}\,s^{-1}\,nm^{-1}$) is the quantity of light available to molecules at a particular location which drives photochemical processes in the atmosphere. The actinic flux may be represented by 3 components: direct radiation, downward diffusive radiation, and upward diffusive radiation. The downward actinic flux is the sum of the direct solar radiation and the downward diffusive radiation, and the net actinic flux is the sum of all 3 components.

To investigate the smoke impact on the actinic fluxes, we selected a location of 33.19N/100.07W, which had both flaming and smoldering smoke cases in the column. Figure 7 shows the calculated downward and net spectral actinic fluxes for flaming and smoldering smoke cases for different times at the smoke plume altitude. Both flaming and smoldering smoke cases have a similar spectral impact on the flux. However, the difference of the actinic flux between 19 and 60 SZA is approximately 2 times larger for the flaming case than for the smoldering smoke case, which illustrates that light scattering/absorption of flaming smoke is sensitive to solar angle.

Figure 8 shows the changes of spectral actinic fluxes ($\Delta F(\lambda)$) for flaming and smoldering types of smoke at different SZAs. Here, we define the change of fluxes as follows:

$$\Delta F(\lambda) = F_{aerosol}(\lambda) - F_{no\ aerosol}(\lambda)$$

A positive ΔF indicates enhanced actinic flux, and negative ΔF indicates reduced actinic flux due to smoke. The type of smoke has different impacts on the radiative forcing in terms of a transition point where $\Delta F = 0$. At the location of 31.04N and 93.23W at 4.5 km (located above the smoke plume height), the flaming smoke reduces actinic fluxes at UV wavelengths and increases the flux at visible wavelengths. The wavelength of the transition point of ΔF becomes shorter with increasing solar angle in the flaming case, which means the flaming smoke aerosol cause more diffusive radiation by the light scattering at the larger solar angle. The impact of smoldering smoke on the flux is relatively small at this location due to the low AOD (<0.1), resulting in small ΔF. At visible wavelengths, ΔF is positive at small solar angle (SZA = 17.783) and negative with increasing solar angle, indicating that the light absorption by aerosols dominates.

The impact of smoke at selected wavelengths is illustrated in Figure 9. It shows the vertical profile of ΔF at 13:20 LT for flaming and smoldering cases. Flaming smoke was loaded at 2 to 4 km at of 31.04N and 93.23W, and ΔF values increase above the smoke altitude. The flaming smoke case has an impact more than 10 times larger than for smoldering smoke. While actinic fluxes are reduced in the UV wavelength, actinic fluxes are increased in the visible wavelength due to absorption by OC. Also, the flaming smoke case significantly changes the actinic flux with altitudes because the flaming smoke is loaded above the boundary layer.

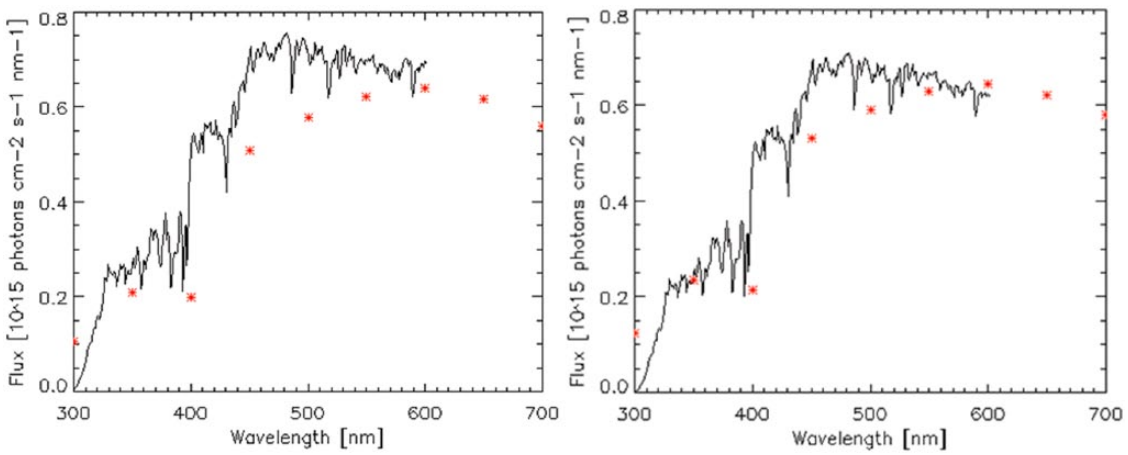

Figure 6. Net actinic fluxes from the aircraft (black line) and from the calculation (red star) for a location in box (a) (left) and box (b) (right).

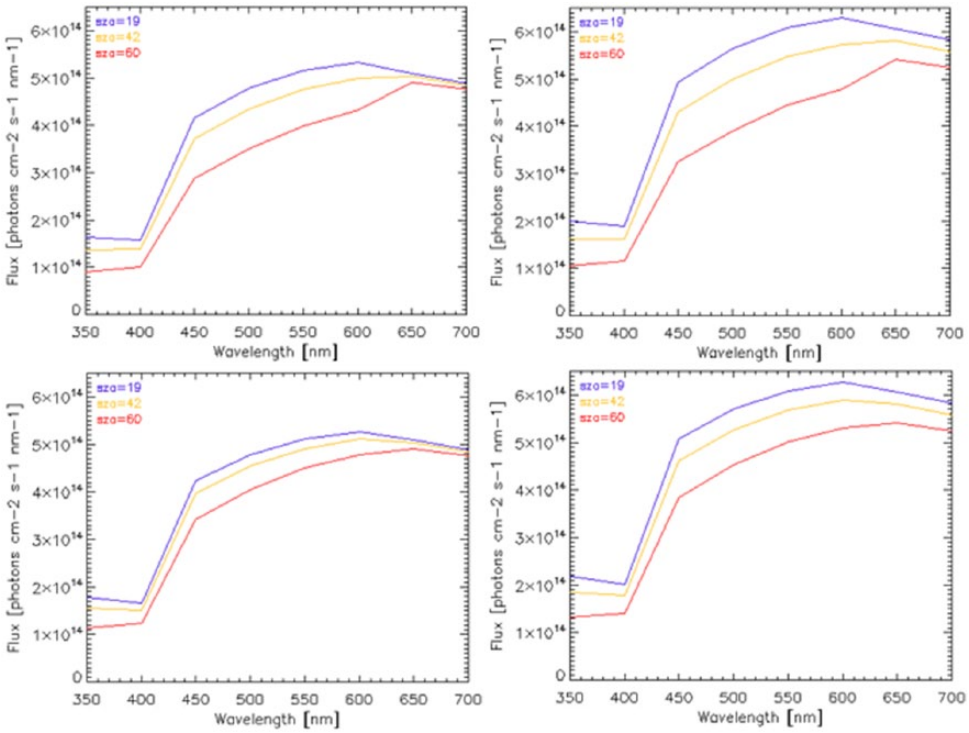

Figure 7. Spectral actinic fluxes (downward: left, total: right) for the flaming smoke case (top) and the smoldering smoke case (bottom) at 33.19N, 100.07W at 0.5 km) for different times (UTC).

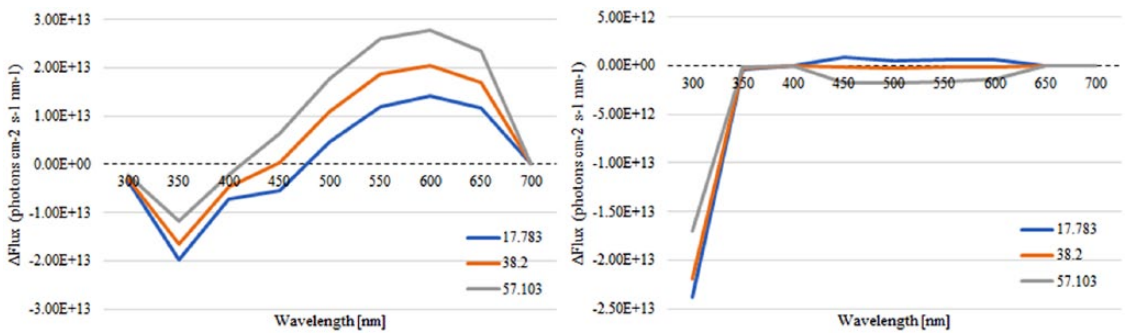

Figure 8. The change of spectral actinic fluxes (total) caused by flaming smoke (left) and smoldering smoke (right) (31.04N, 93.23W above smoke height [5 km for flaming and 0.2 km for smoldering smoke]) for different solar zenith angles (SZA = 17.783°, 38.2°, and 57.103°).

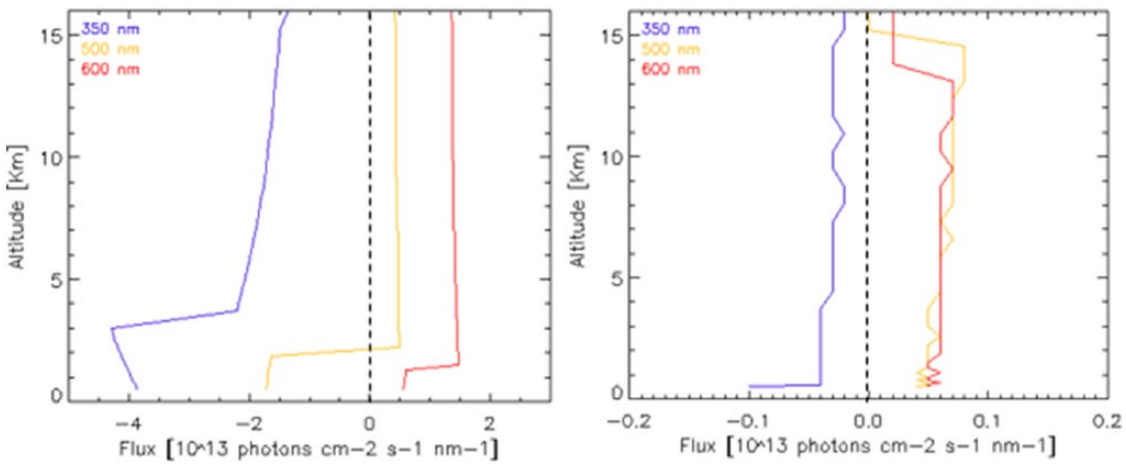

Figure 9. Vertical profiles of ΔF for flaming smoke (left) and smoldering smoke (right) (31.04N 93.23W) for the different wavelengths at SZA = 17.78°.

Conclusions

In this study, we have investigated the effects of smoke aerosols on UV and visible actinic fluxes by computing and examining the spectral optical properties of smoke according to different compositions. We defined 2 representative smoke regimes, flaming and smoldering, consisting of OC, BC, and SO4. The spectral optical properties were calculated for each smoke type, from its corresponding refractive index and size distribution. Then, the optics of external mixtures was computed by summing up the weighed optical properties of individual species. The calculated optical properties of each smoke regime were incorporated into the TUV model to compute spectral actinic fluxes.

Here is a brief summary of the main findings from this study. (1) The WRF-Chem-SMOKE model was used to simulate biomass burning aerosols from smoke plumes using fire emission data. However, the smoke field has some uncertainty, including somewhat low AOD values due to insufficient fire emissions and incorrect spatial distribution of aerosols due to errors of meteorological variables (especially, wind speed and direction). Adjusting the fire size for the emission inputs is required to improve the simulation, as well as improving meteorological fields. (2) From the analysis of smoke optical properties, the SSA from flaming fires is higher than from smoldering fires due to the fraction of nonabsorbing SO_4 component of flaming smoke. The main difference of the smoke component fraction between flaming and smoldering smoke cases is OC and SO_4, which are well activated in the aged smoke case as they have more time to be oxidized. (3) From the comparison of the fluxes with the observation data, the simulated actinic flux was underestimated at the selected locations. The simulated flaming smoke is loaded at 2 to 4 km at the 2 locations, but the altitude of the flux for comparison is around 7 km where the aircraft is located. Thus, further analysis related to injection height may be required to reduce the current uncertainty of the net actinic flux from the simulation. In addition, the model considers only available aerosols due to biomass burning but the measured actinic flux may be affected by other aerosols from natural and anthropogenic sources. (4) The type of smoke has different impacts on the actinic flux and thus the spectral radiative forcing. From the selected locations, the flaming smoke reduces actinic fluxes at UV wavelengths and increases the flux at the visible wavelengths. The flaming smoke aerosol increases diffusive radiation due to higher scattering, particularly at the larger solar angle. However, the impact of smoldering smoke on the flux is relatively small at this location due to the low AOD. As SZA increases, the light absorption by aerosols dominates and reduces photochemical processes. However, this conclusion may be changed depending on locations because the case study is limited to certain locations.

From the analysis of the spectral actinic fluxes, it is apparent that the smoke impact on the radiative forcing depends on smoke types and the fraction of smoke components, which influence optical properties. The spectral refractive index and size distribution are key parameters to determine spectral smoke optical properties. Because the impact of smoke on the UV and visible spectra varies with smoke properties (the smoke phase, smoke intensity, and fuel type, and smoke injection height, etc), our approach shows the importance of spectral optical properties in the modeling of the smoke radiative impact.

REFERENCES

1. IPCC. *Climate Change 2007: The Physical Science Basis. Contribution of Working Group I to the Fourth Assessment Report of the Intergovernmental Panel on Climate Change* (ed Solomon S, Qin D, Manning M, et al.). Cambridge and New York: Cambridge University Press; 2007.
2. Schwartz SE. The white house effect—shortwave radiative forcing of climate by anthropogenic aerosols: an overview. *J Aerosol Sci*. 1996;27:359–382.
3. Hansen J, Sato M, Ruedy R. Radiative forcing and climate response. *J Geophys Res*. 1997;102:6831–6864.
4. Holben BN, Eck TF, Slutsker I, et al. AERONET—a federated instrument network and data archive for aerosol characterization. *Remote Sens Environ*. 1998;66:116.
5. Cook J, Highwood EJ. Climate response to tropospheric absorbing aerosols in an intermediate general-circulation model. *Q J R Meteorol Soc*. 2004;130:175–191.
6. Chameides WL, Yu H, Liu SC, et al. Case study of the effects of atmospheric aerosols and regional haze on agriculture: an opportunity to enhance crop yields in China through emission controls? *Proc Natl Acad Sci U S A*. 1999;96:13626–13633.

7. Cohan DS, Xu J, Greenwald R, Bergin MH, Chameides WL. Impact of atmospheric aerosol light scattering and absorption on terrestrial net primary production, Global Biogeochem. *Cycles*. 2002;16:37-1–37-12.
8. Gu L, Baldocchi D, Verma SB, et al. Advantages of diffuse radiation for terrestrial ecosystem productivity. *J Geophys Res*. 2002;107:4050.
9. Gu L, Baldocchi DG, Wofsy SC, et al. Response of a deciduous forest to the Mount Pinatubo eruption: enhanced photosynthesis. *Science*. 2003;299: 2035–2038.
10. Kobayashi H, Matsunaga T, Hoyano A, Aoki M, Komori D, Boonyawat S. Satellite estimation of photosynthetically active radiation in Southeast Asia: impacts of smoke and cloud cover. *J Geophys Res*. 2004;109:D04102.
11. Li G, Bei N, Tie X, Molina LT. Aerosol effects on the photochemistry in Mexico City during MCMA-2006/MILAGRO campaign. *Atmos Chem Phys*. 2011;11:5169–5182.
12. Kirchstetter TW, Novakov T, Hobbs PV. Evidence that the spectral dependence of light absorption by aerosols is affected by organic carbon. *J Geophys Res*. 2004;109:D21208.
13. Lewis K, Arnott WP, Moosmüller H, Wold CE. Strong spectral variation of biomass smoke light absorption and single scattering albedo observed with a novel dual-wavelength photoacoustic instrument. *J Geophys Res*. 2008;113:D16203.
14. Reid JS, Eck TF, Christopher SA, et al. A review of biomass burning emissions part III: intensive optical properties of biomass burning particles. *Atmos Chem Phys*. 2005;5:827–849.
15. Ohlemiller TJ. Smoldering combustion. In: DiNenno PJ, Drysdale D, Bayler CL, Walton WD, eds. *The SFPE Handbook of Fire Protection Engineering*, 3rd ed. Quincy, MA: National Protection Fire Association; 2002:581–603.
16. Val Martin M, Kahn RA, Logan JA, Paugam R, Wooster M, Ichoku C. Space-based observational constraints for 1-D fire smoke plume-rise models. *J Geophys Res*. 2012;117:D22204.
17. Freeborn PH, Wooster MJ, Roy DP, Cochrane MA. Quantification of MODIS fire radiative power (FRP) measurement uncertainty for use in satellite-based active fire characterization and biomass burning estimation. *Geophys Res Lett*. 2014;41:1988–1994.
18. Kauffman JB, Cummings DL, Ward DE. Fire in the Brazilian Amazon 2. Biomass, nutrient pools and losses in cattle pastures. *Oecologia*. 1998;113(3):415–427. doi:10.1007/s004420050394
19. Lee SC, Tien CL. *Eighteenth Symposium (International) on Combustion*. Pittsburgh, PA: The Combustion Institute; 1981:1159–1166.
20. Chang H, Charalampopoulos TT. Determination of the wavelength dependence of refractive indices of flame soot. *Proc R Soc*. 1990;430:577–591.
21. Massie ST, Hervig M. HITRAN 2012 refractive indices. *J Quant Spec Rad Trans*. 2013;180:373–380.
22. Reid JS, Koppmann R, Eck TF, Eleuterio DP. A review of biomass burning emissions part II: intensive physical properties of biomass burning particles. *Atmos Chem Phys*. 2005;5:799–825.
23. Fast JD, Gustafson WI Jr, Easter RC, et al. Evolution of ozone, particulate, and aerosol direct radiative forcing in the vicinity of Houston using a fully coupled meteorology-chemistry-aerosol model. *J Geophys Res*. 2006;111:D21305.
24. Tuccella P, Curci G, Visconti G, Bessagnet B, Menut L, Park RJ. Modeling of gas and aerosol with WRF/Chem over Europe: evaluation and sensitivity study. *J Geophys Res*. 2012;117:D03303.
25. Zhao C, Liu X, Leung LR, et al. The spatial distribution of mineral dust and its shortwave radiative forcing over North Africa: modeling sensitivities to dust emissions and aerosol size treatments. *Atmos Chem Phys*. 2010;10:8821–8838.
26. Wang J, Ge C, Yang Z, et al. Mesoscale modeling of smoke transport over the Southeast Asian Maritime Continent: interplay of sea breeze, trade wind, typhoon, and topography. *Atmos Res*. 2013;122:486–503.
27. Ackermann IJ, Hass H, Memmesheimer M, Ebel A, Binkowski F, Shankar U. Modal aerosol dynamics model for Europe: development and first applications. *Atmos Environ*. 1998;17:2981–2999.
28. Schell B, Ackermann IJ, Hass H, Binkowski FS, Ebel A. Modeling the formation of secondary organic aerosol within a comprehensive air quality model system. *J Geophys Res*. 2001;106:28275–28293.
29. Madronich S, Flocke S. The role of solar radiation in atmospheric chemistry. In: Boule P, ed. *Handbook of Environmental Chemistry*. Heidelberg: Springer; 1999:1–26.
30. Katsaros KB, McMurdie LA, Lind RJ, DeVault JE. Albedo of a water surface, spectral variation, effects of atmospheric transmittance, sun angle, and wind speed. *J Geophys Res*. 1985;90:7313–7321.
31. Feister U, Grewe R. Spectral albedo measurements in the UV and visible region over different types of surfaces. *Photochem Photobiol*. 1995;62:736–744.
32. Freitas SR, Longo KM, Alonso MF, et al. PREP-CHEM-SRC 1.0: a preprocessor of trace gas and aerosol emission fields for regional and global atmospheric chemistry models. *Geosci Model Dev*. 2011;4:419–433.
33. Sessions WR, Fuelberg H, Kahn R, Winker D. An investigation of methods for injecting emissions from boreal wildfires using WRF-Chem during ARCTAS. *Atmos Chem Phys*. 2011;11:5719–5744.